UC San Diego
UC San Diego Previously Published Works

Title
Solution-Processed Phototransistors Combining Organic Absorber and Charge Transporting Oxide for Visible to Infrared Light Detection.

Permalink
https://escholarship.org/uc/item/6v11s2zp

Journal
ACS applied materials & interfaces, 11(40)

ISSN
1944-8244

Authors
Kim, Hyonwoong
Wu, Zhenghui
Eedugurala, Naresh
et al.

Publication Date
2019-10-01

DOI
10.1021/acsami.9b08622

Peer reviewed

eScholarship.org Powered by the California Digital Library
University of California

ACS APPLIED MATERIALS & INTERFACES

Research Article

Cite This: ACS Appl. Mater. Interfaces 2019, 11, 36880−36885

www.acsami.org

Solution-Processed Phototransistors Combining Organic Absorber and Charge Transporting Oxide for Visible to Infrared Light Detection

Hyonwoong Kim,[†,‡] Zhenghui Wu,[†] Naresh Eedugurala,[§] Jason D. Azoulay,[§] and Tse Nga Ng*[,†,‡]

[†]Department of Electrical and Computer Engineering and [‡]Materials Science and Engineering Program, University of California San Diego, 9500 Gilman Drive, La Jolla, California 92093, United States

[§]Center for Optoelectronic Materials and Devices, School of Polymer Science and Engineering, The University of Southern Mississippi, 118 College Drive, No. 5050, Hattiesburg, Mississippi 39406, United States

Supporting Information

ABSTRACT: This report demonstrates high-performance infrared phototransistors that use a broad-band absorbing organic bulk heterojunction (BHJ) layer responsive from the visible to the shortwave infrared, from 500 to 1400 nm. The device structure is based on a bilayer transistor channel that decouples charge photogeneration and transport, enabling independent optimization of each process. The organic BHJ layer is improved by incorporating camphor, a highly polarizable additive that increases carrier lifetime. An indium zinc oxide transport layer with high electron mobility is employed for rapid charge transport. As a result, the phototransistors achieve a dynamic range of 127 dB and reach a specific detectivity of 5×10^{12} Jones under a low power illumination of 20 nW/cm^2, outperforming commercial germanium photodiodes in the spectral range below 1300 nm. The photodetector metrics are measured with respect to the applied voltage, incident light power, and temporal bandwidth, demonstrating operation at a video-frame rate of 50 Hz. In particular, the frequency and light dependence of the phototransistor characteristics are analyzed to understand the change in photoconductive gain under different working conditions.

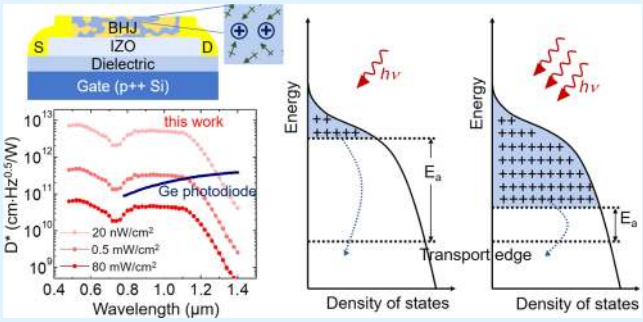

KEYWORDS: *shortwave infrared, phototransistor, carrier lifetime, semiconducting polymer, indium zinc oxide, bulk heterojunction, camphor*

INTRODUCTION

Organic semiconductors offer highly tunable optoelectronic properties and the advantages of economically large-area deposition and low-temperature processing. In particular, solution-processed semiconducting polymers are being developed, which extend the spectral range of these materials beyond the visible, to enable scalable large-area photodetectors responsive to near-infrared (NIR: 0.75−1 μm) and shortwave infrared (SWIR: 1−3 μm) radiation.[1,2] Infrared light detection provides additional information beyond visible light in biomedical and military applications, as infrared light can offer higher contrast and deeper penetration depth compared to visible wavelengths.[3]

As the band gap of the materials is further reduced for infrared detection,[4,5] the device performance becomes increasingly restricted by the nonradiative recombination[6,7] of photogenerated carriers. Charge recombination may occur during the exciton dissociation step or during charge transport, and optimization of each step is desirable but complicated in bulk heterojunction (BHJ) architectures. In BHJ photodiodes, a large interfacial area between the donor and acceptor components facilitates exciton dissociation into free carriers, which must then navigate interpenetrating donor and acceptor phase-separated domains to reach their respective electrodes. The nature of the interfaces, structural and energetic heterogeneities, and disordered domains impede carrier transport within these systems. As such, it has been challenging to address the conflicting requirements in a single active layer.[8−12] As an alternative, bilayer phototransistor structures[13−19] are being designed to decouple both materials and processes associated with charge photogeneration and transport to improve device performance.

The phototransistor structures here address the recombination issue and enhance photoconductive gain using separate layers for charge photogeneration and transport. Phototransistors use the applied electric field from the gate electrode to promote photoconductive gain. The gain mechanism[20−23] originates from trap states within the semiconductor band gap.

Received: May 17, 2019
Accepted: September 16, 2019
Published: September 16, 2019

Downloaded via UNIV OF CALIFORNIA SAN DIEGO on October 10, 2019 at 16:47:32 (UTC).
See https://pubs.acs.org/sharingguidelines for options on how to legitimately share published articles.

© 2019 American Chemical Society

DOI: 10.1021/acsami.9b08622
ACS Appl. Mater. Interfaces 2019, 11, 36880−36885

After photogeneration of electron−hole pairs, one carrier type is captured and localized in the traps. The opposite carrier type is collected and also injected under bias between the source and drain electrodes, due to the electric field from the trapped charges. Within the trapped carrier lifetime, injected carriers circulate multiple times, leading to amplification of the photocurrent and external quantum efficiency (EQE) exceeding 100%. The photoconductive gain is proportional to the ratio of $\tau_{trap}/\tau_{transit}$, where τ_{trap} is the trapped carrier lifetime and $\tau_{transit}$ is the transit time across the transistor channel. Thus extending the carrier lifetime and reducing transit time are needed to increase gain.

In our bilayer phototransistors, the photogeneration materials are chosen to be responsive to infrared wavelengths (λ) out to 1400 nm. Compared to inorganic semiconductors, organic semiconductors show relatively small permittivity,[24,25] which is inversely proportional to the exciton binding energy and affects charge generation. Since the probability of recombination increases in narrow band-gap IR materials, here, we tune the organic BHJ layer with a high-permittivity molecule camphor[26,27] to assess whether the polarizable additive would stabilize photogenerated charge and improve carrier lifetimes.

In our system, the photogenerated holes are trapped in the BHJ, while electrons circulate in the transport layer consisting of inkjet printed indium zinc oxide (IZO),[28,29] which offers higher mobility than organic materials and the potential for low-cost, large-area integration in pixelated imagers.[13,30] The key photodetector characteristics, including temporal bandwidth, detectivity, photoconductive gain, and dynamic range, are analyzed for two compositions at various operational voltages and bandwidths. To ensure correct characterization, we pay attention to the frequency and light dependence of the phototransistor characteristics, to understand the change in photoconductive gain under different working conditions. This novel IR phototransistor design is shown to exceed the performance of commercial vacuum-processed germanium photodiodes at video rate spanning the visible to the shortwave IR ($500 < \lambda < 1300$ nm) under low light illumination.

RESULTS AND DISCUSSION

Figure 1a shows the chemical structures of the materials in the BHJ layer, which includes a blend of a narrow band-gap IR absorbing polymer (poly(4-(5-(4-(3,5-bis(dodecyloxy)-benzylidene)-4*H*-cyclopenta[2,1-*b*:3,4-*b*′]dithiophen-2-yl)-thiophen-2-yl)-6,7-dioctyl-9-(thiophen-2-yl)-[1,2,5]-thiadiazolo[3,4-*g*]quinoxaline)) as the donor[26] and [6,6]-phenyl-C_{71}-butyric acid methyl ester ($PC_{71}BM$) as the acceptor. The donor-to-acceptor ratio is 1:2 by weight, and devices are fabricated with or without camphor as the high-permittivity additive. Camphor is an insulating organic molecule, and adding it to the BHJs has been shown to increase the dielectric constant of BHJs and facilitate charge dissociation,[26,27] which, in particular, is a bottleneck for organic infrared devices (less so for wider band-gap photovoltaics). For films with camphor (1,7,7-trimethylbicyclo[2.2.1]heptan-2-one((±)-camphor)), the weight percentage of the additive is 23%.[27,31] The atomic force microscopy measurements in Supporting Information Figure S1 show that the BHJ film morphology change on the surface is not observed upon adding camphor. The absorption spectra of BHJ materials show no significant spectral shift upon camphor addition. The BHJ absorption spectra and electrochemical measurements used to determine the polymer energy levels are included in the Supporting Information (Figure S1).

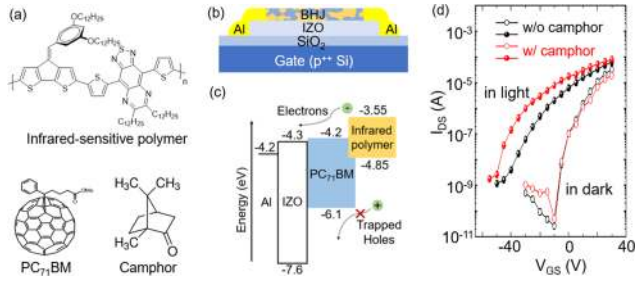

Figure 1. (a) Chemical structures of materials in the bulk heterojunction (BHJ) layer. (b) Phototransistor structure with indium zinc oxide (IZO) as the electron transporting layer. (c) Energy diagram illustrating electron transfer from the BHJ to IZO, whereas holes are trapped in BHJ. (d) Current−voltage characteristics of phototransistors at V_{DS} = 5 V. Open symbols: measured in the dark; solid symbols: measured under light. The light was from an light-emitting diode (LED) emitting at a 940 nm wavelength with a power of 50 mW/cm^2.

Figure 1b illustrates the phototransistor structure in a bottom-gate, top-contact configuration. The effective mobility of IZO transistors before BHJ deposition is measured to be 0.83 ± 0.07 cm^2/(V s) at saturation, as shown in Supporting Information Figure S2. The energy band diagram for the combination of a BHJ layer on top of an IZO transport channel is depicted in Figure 1c. IZO is a wide band-gap material that does not show photoresponse in the IR (Supporting Information Figure S2), and the organic BHJ is responsible for infrared photogeneration. Under illumination, incident photons generate excitons, which are dissociated into electrons and holes at donor−acceptor interfaces in the BHJ. Due to the energy barrier for holes, holes are trapped[14,32] in the BHJ, while electrons are spontaneously transferred to the IZO channel (schematics in Supporting Information Figure S2). As a result, injected electrons circulate multiple times across the transistor channel until the holes recombine, inducing photoconductive gain.

Figure 1d shows the current−voltage characteristics of the BHJ−IZO phototransistors. The phototransistor output characteristics and comparisons to alternative device structures, such as a single-layer BHJ without IZO, or a planar junction instead of a BHJ, are included in Supporting Information Figure S3. In the dark, the BHJ−IZO devices show a similar turn-on voltage V_{on} = −10 V, with or without camphor. On the other hand, under λ = 940 nm irradiation of 50 mW/cm^2, the V_{on} shifts in the negative direction due to trapped holes, changing by 40 V for the device with camphor and by 34 V for the one without camphor. The photocurrent, which is $I_{ph} = I_{light} - I_{dark}$, is higher for the device with camphor across all gate voltages.

To investigate how the camphor additive increases photocurrent, the phototransistors are analyzed through electrochemical impedance spectroscopy under different illumination power, as shown in Figure 2a,b. The source and drain electrodes are connected to the potentiostat, while a sinusoidal waveform with a 100 mV amplitude is applied over a frequency range of 100 Hz to 2 MHz. These measurements do not differentiate between electrons and holes and report their average lifetime before recombination. The Nyquist plots are fitted to an equivalent circuit[33] with components of shunt

DOI: 10.1021/acsami.9b08622
ACS Appl. Mater. Interfaces 2019, 11, 36880−36885

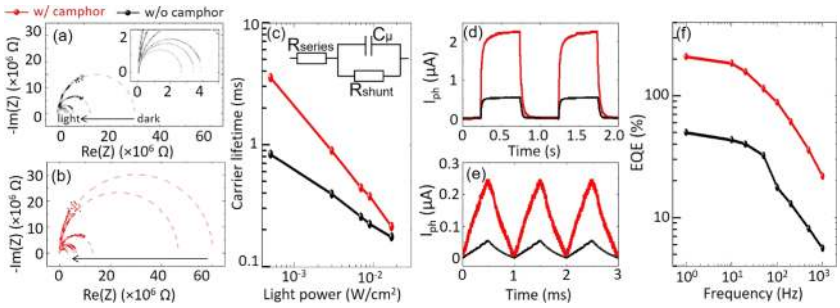

Figure 2. Nyquist plots of phototransistors in which the BHJ is (a) without camphor (black) versus (b) with camphor (red). Measurements were taken in the dark and under light power of 0.5, 3, 7, 9, and 17 mW/cm^2. Arrows point in the direction of increasing light intensity. The inset in part (a) zooms in on the measurements under 7, 9, and 17 mW/cm^2. Dashed lines indicate fits to the equivalent circuit shown in the inset of (c). (c) Carrier lifetime versus incident light power. Photocurrent versus time, as the incident light is switched on and off at frequencies of (d) 1 Hz and (e) 1 kHz. (f) External quantum efficiency versus temporal bandwidth. Parts (d)−(f) are measured at $V_{GS} = -10$ V and $V_{DS} = 5$ V, under a light power of 5 mW/cm^2 at a 940 nm wavelength.

resistance R_{shunt} and capacitance C in parallel, which are in series with series resistance R_{series}. The fit values of $R_{shunt} \times C$ are estimates of the carrier lifetime, displayed in Figure 2c. The carrier lifetime is consistently longer in the BHJ with camphor than in the film without camphor, in agreement with prior work[25,26] that high-permittivity environment can stabilize free carriers. Furthermore, in the following analysis, we will characterize the effects of camphor additives on improving photoconductive gain.

Characteristics with Respect to Sampling Frequencies. The photocurrent in Figure 2d,e shows the effects of photoconductive gain with time, as incident light pulses are modulated at different temporal frequencies. When the light source is switched on and off at 1 kHz in Figure 2e, the photocurrent shows a monotonic rise and fall. The I_{ph} is amplified by the photoconductive gain mechanism due to the trapped holes in the BHJ. Due to the electric field from the trapped holes, electrons are injected into the transistor channel, resulting in a circulation of electrons that amplify the photocurrent over time.

The photoconductive gain is proportional to the light pulse duration. At a slow frequency of 1 Hz in Figure 2d, the photocurrent reaches a plateau, and the maximum gain is dictated by the equilibrium between the circulation time of injected electrons and the detrapping time of photogenerated holes. In the dark, the bilayer transistors show a rise/fall time of <150 μs, as V_{DS} is switched (Supporting Information Figure S4). Thus, the charging/discharge time of the transistor channel is significantly shorter than the recirculation time [in tens of milliseconds in Figure 2d,e] due to photoconductive gain, and the photocurrent is not influenced by the charging time.

The phototransistors are operated at a certain duty cycle. The on−off duty cycle will be chosen depending on the application requirements; if the low frequency is allowed, the longer time period will allow the electrons to recirculate more rounds and increase the photoconductive gain until an equilibrium is established between electron recirculation and hole detrapping, as shown in Figure 2d. As the photocurrent is the difference of $I_{ph} = I_{light} - I_{dark}$, the drift in dark current due to bias stress[14,32] does not significantly affect the differential signal. The percentage change of photocurrent over 10 min is determined to be less than 5% in Supporting Information Figure S5, indicating stable photodetecting performance.

The external quantum efficiency (EQE) increases with lower light modulation frequency as seen in Figure 2f. The EQE is calculated from the equation

$$\mathrm{EQE} = (I_{ph} \times h \times c)/(q \times P_{inc} \times \lambda) = R(h \times c)/(q \times \lambda) \quad (1)$$

where h is Planck's constant, c is the speed of light, q is the charge, P_{inc} is the incident light power, λ is the incident light wavelength, and $R = I_{ph}/P_{inc}$ is the responsivity in the unit of ampere per watt. The photocurrent I_{ph} is the value at the end of an illumination cycle. The EQE starts to decrease around 50 Hz, as there is less time for electrons to recirculate and amplify the photocurrent through photoconductive gain. Nonetheless, the roll-off frequency of 50 Hz allows video rate recording.

In general, the photocurrent measured in Figure 2 increases with camphor additive, because the trapped holes show longer lifetime and lead to a higher electric field than in devices without camphor. As a side note, it is observed that the photocurrent rise/decay time in temporal responses is different by an order of magnitude from the carrier lifetime obtained from the Nyquist plots. Carrier lifetime in Figure 2a,b only reflects the time taken for excess carrier recombination via band-to-band or trap-assisted recombination. In devices with photoconductive gain, the photocurrent decay time is determined by the detrapping time of the trapped carriers, which is at a longer time scale than recombination.[23,34] While a long τ_{trap} can result in persistent photoconductivity, switching the gate bias to recombine the trapped charges[30] will increase the refresh rate.

Characteristics with Respect to Applied Voltages. In addition to dependence on the operational frequency, the photocurrent and EQE are dependent on the applied gate bias V_{GS}. As the phototransistor gate bias switches the channel from the depletion to the accumulation regime, the EQE increases up to ∼1000%, as shown in Figure 3a. In the accumulation regime, the positive gate bias attracts electrons to the IZO channel, resulting in high effective mobility and raising photocurrent. In the depletion regime, the negative gate bias depletes the IZO channel, lowering the mobility and photoconductive gain. The photocurrent is shown to be linearly proportional to source−drain bias V_{DS} (Supporting Information Figure S6), complying to the relation[13]

DOI: 10.1021/acsami.9b08622
ACS Appl. Mater. Interfaces 2019, 11, 36880−36885

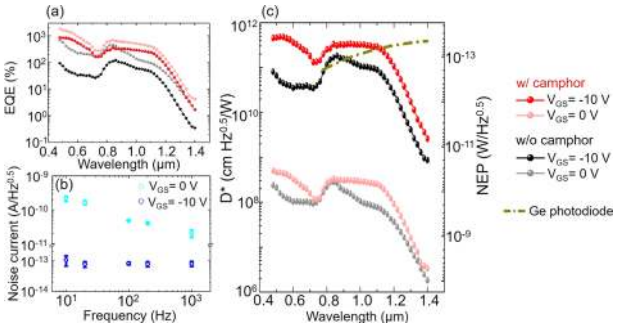

Figure 3. (a) External quantum efficiency versus incident light wavelength, for phototransistors with or without camphor and operating under different gate bias conditions. (b) Noise current in the dark under different gate bias conditions versus frequency. (c) Detectivity and noise-equivalent power of the phototransistors versus incident light wavelength. The source−drain bias is fixed at 5 V, and the incident light is 0.3−0.5 mW/cm^2, modulated at a frequency of 10 Hz. The commercial germanium photodiode part number is 818-IR from Newport Corporation.

$$I_{ph} = q \times A \times G_0 \times \tau_{trap}/\tau_{transit} = q \times A \times G_0 \times \tau_{trap}(\mu \times V_{DS}/L^2) \quad (2)$$

where A is the photosensor area, G_0 is the generation rate, μ is the effective field-effect mobility in the IZO channel, and L is the channel length. The transit time $\tau_{transit}$ can be reduced by decreasing the channel length or increasing the mobility or source−drain bias. The lower bound for τ_{trap} is the carrier lifetime in Figure 2c. Compared to the device without camphor, the phototransistor with camphor retains trapped holes longer, leading to higher EQE across the spectral range.

Higher V_{GS} increases EQE but also the dark current noise, as seen in Figure 3b. There is negligible difference in dark current between devices with or without camphor in the BHJ, indicating that noise is dominated by the shot noise in the transport channel, which is the same for both types of devices. For comparison, infrared photodiodes operating without an external bias are dominated by thermal noise.[5] However, here, the devices are under bias, and shot noise or flicker noise can overtake the thermal noise component depending on the operational bias and frequency. The measured noise in the accumulation regime (V_{GS} = 0 V) is almost two orders of magnitude higher than in the depletion regime (V_{GS} = −10 V), as shot noise[35] is proportional to the square root of current density.

The highest signal-to-noise ratio, or detectivity, is observed at the turn-on voltage in the dark, namely, at V_{GS} = −10 V in Figure 1d. The specific detectivity[35] is

$$D^* = (A \times \Delta f)^{0.5}/\mathrm{NEP} = (A \times \Delta f)^{0.5}(R/i_{noise}) \quad (3)$$

where A is the photosensor area, Δf is the temporal bandwidth, and NEP is the noise-equivalent power defined as responsivity R divided by noise current i_{noise}. Figure 3c displays the specific detectivity and noise-equivalent power calculated using measurement values from Figure 3a,b. The best detectivity is obtained from the phototransistor with camphor operating in the depletion regime at V_{GS} = −10 V, and this device shows detectivity that surpasses a commercial germanium photodiode (818-IR, Newport Corporation) in the IR region between 800 and 1300 nm, depending on light power as shown in Figure 4.

Characteristics with Respect to the Incident Light Power. Another metric for photodetectors is the dynamic range, which indicates the range of incident light power that the photodetector can respond to and is defined as DR = $20\log(P_{inc,max}/P_{inc,min})$, where $P_{inc,max}$ is the maximum light power before saturation and $P_{inc,min}$ is the minimum light power detectable above the noise level. From Figure 4, the dynamic range is estimated to be 127 dB for the phototransistor with camphor and 116 dB for the device without camphor. The superior dynamic range in the device with camphor is due to the lower detection limit from higher photoconductive gain.

In phototransistors, the photoconductive gain leads to a nonconstant responsivity versus incident light power in Figure 4, which contrasts with typical photodiodes in which responsivity remains constant with incident light power. In phototransistors, as the incident light power increases, the responsivity decreases because of the distribution of trap states.[20] The photogenerated carriers occupy deep traps first under low light power. The charges in deep traps are slow to escape from the traps due to high activation energy E_a, leading to long τ_{trap} and high photoconductive gain and responsivity. Under high light power, the deep trap states are already filled and shallow trap states start to dominate the photodetector response. The shallow traps allow faster detrapping kinetics, resulting in lower τ_{trap} and reduced responsivity. Comparisons between devices with photoconductive gain need to take the light intensity into account; some of the reported high responsivity values and thus high resolution will be valid only at low light levels. As such, the phototransistors are more sensitive at lower incident light power.

■ CONCLUSIONS

The phototransistors here achieve high-performance, broadband spectral response through the effective combination of BHJ for photogeneration and IZO for charge transport. This bilayer design allows independent optimization of each layer. The BHJ is improved with high-permittivity camphor to

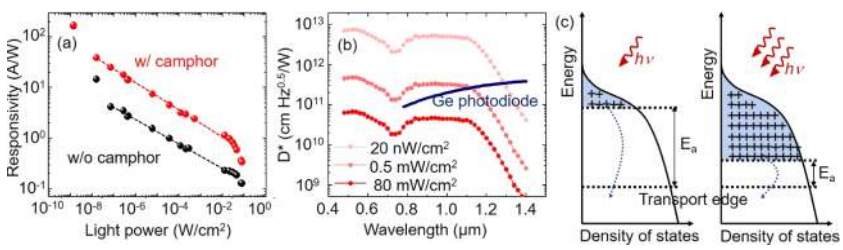

Figure 4. (a) Responsivity and (b) detectivity as a function of incident light power. The phototransistor with camphor (data in red) is biased at V_{GS} = −10 V, V_{DS} = 5 V, and the light source is modulated at 10 Hz from an LED at a 940 nm wavelength. The blue line indicates commercial germanium photodiode. (c) Schematic diagram of trap occupancy under different light power.

DOI: 10.1021/acsami.9b08622
ACS Appl. Mater. Interfaces 2019, 11, 36880−36885

increase the trapped carrier lifetime, while the IZO layer maintains short carrier transit time. The photogeneration layer can be tuned using different photosensitive polymers for different spectral ranges, and this work uses an infrared-sensitive polymer that is responsive in the visible to the infrared, from 500 to 1400 nm.

We examine the device characteristics with respect to operational frequency, applied bias, and incident light intensity, to analyze the dependence of photoconductive gain on these three factors. The devices show peak performance at low illumination power, with the applied gate bias in the depletion regime near the turn-on voltage, and at switching frequencies that allow sufficient time for electron recirculation to maximize photoconductive gain. By understanding these dependences, the phototransistor noise is minimized, and the devices are shown to achieve a detectivity of up to 5×10^{12} cm $Hz^{0.5}$/W under an incident light of 20 nW/cm^2 and allow operation at a video-frame rate of 50 Hz. This excellent performance shows that the solution-processed infrared phototransistors here provide a path to realize affordable large-area infrared imagers crucial to many spectroscopic applications.

EXPERIMENTAL PROCEDURES

Phototransistor Fabrication. A heavily p-doped Si wafer with a 300 nm thermal oxide was UV−ozone-treated for 5 min to remove organic residue and enhance the wettability. The IZO ink consisted of 0.12 M of indium nitrate hydrate and 0.08 M of zinc nitrate hexahydrate in 2-methoxyethanol.[28,29] The IZO precursor solution was printed using inkjet[36] (Fujifilm Dimatix DMP2800), with the substrate heated at 60 °C. The printed IZO film was annealed at 400 °C in air for 2 h. For contact electrodes, 40 nm aluminum was thermally deposited in a $\sim 2 \times 10^{-6}$ mbar vacuum. Aluminum was used to match the work function for electron injection/extraction and reducing hole injection/extraction. The transistor channel dimension was 30 μm length × 1000 μm width.

The BHJ solution was prepared by mixing 1 mg/mL of donor polymer and 2 mg/mL of $PC_{71}BM$ (>99%, Ossila) in toluene with 3 vol % of diiodooctane (98%, Sigma-Aldrich). The synthesis procedure for the donor polymer is found in the Supporting Information and in refs 26, 37. For films with 1,7,7-trimethylbicyclo[2.2.1]heptan-2-one((±)-camphor) (Sigma-Aldrich), the desired weight percentage is added to the BHJ solution (Supporting Information Figure S7). Prior to BHJ deposition, the IZO thin-film transistor was rinsed with acetone and isopropanol to remove the organic residue and annealed at 120 °C in nitrogen to desorb water molecules. The BHJ solution was spin-coated at 5000 rpm for 60 s and vacuum-dried for 10 min. For encapsulation, the device was sealed with a glass slide bonded with epoxy.

Device Characterization. In the EQE measurements,[38] the monochromatic light source was modulated at 10 Hz by an optical chopper, and the device photocurrent was amplified through a low-noise amplifier (SR570, Stanford Research Systems) and measured with a lock-in amplifier (SRS530, Stanford Research Systems). Filters with cutoff wavelengths of 455, 645, and 1025 nm were used to reduce the scattered light from higher-order diffraction. The incident light power is measured with a Ge photodiode (818-IR, Newport Corporation) for 780−1400 nm range and a Si photodiode (DET36A, Thorlabs) for 460−780 nm. Electrochemical impedance spectroscopy was performed with a potentiostat (SP200, Bio-logic) over the frequency range of 100 Hz to 2 MHz with a 100 mV amplitude,[39] with the phototransistor gate electrode floating.

A lock-in amplifier was used to measure the noise current density. The background noise current external to the device (i.e., preamplifier, leads, etc.) contributed to the total noise current and was measured by connecting the leads with no device in place. The device was connected to the preamplifier at the source and drain electrodes, while external bias voltages were applied to the gate (V_{GS} = 0 or −10 V) and drain electrodes (V_{DS} = 5 V). The background noise was subtracted from the total noise to obtain the device noise. Preamplifier was in low-noise mode, and the noise current density was an average from 10 measurements at each frequency.

To measure the temporal response of phototransistors, a light-emitting diode (LED) with a center wavelength of 940 nm and a spectral width of 50 nm was used as the light source. Light power was tuned by placing neutral density filters over the device. The input voltage waveform to the LED was controlled by a function generator. The transistor photocurrent is converted to voltage through a preamplifier in high bandwidth mode, and the output voltage is recorded by an oscilloscope.

ASSOCIATED CONTENT

Supporting Information

The Supporting Information is available free of charge on the ACS Publications website at DOI: 10.1021/acsami.9b08622.

Semiconducting polymer absorption, energy levels, cyclic voltammetry of the IR-sensitive polymer, and atomic force microscopy data; phototransistor structures and device stability characterization; representative current−voltage characteristics of indium zinc oxide (IZO) transistors in the dark, showing negligible hysteresis (PDF)

AUTHOR INFORMATION

Corresponding Author

*E-mail: tnn046@ucsd.edu.

ORCID

Zhenghui Wu: 0000-0002-4187-9280
Naresh Eedugurala: 0000-0003-4714-7993
Jason D. Azoulay: 0000-0003-0138-5961
Tse Nga Ng: 0000-0001-6967-559X

Notes

The authors declare no competing financial interest.

ACKNOWLEDGMENTS

H.K., Z.W., and T.N.N. are grateful for the support from the National Science Foundation (NSF ECCS-1839361). Part of the work was performed at the San Diego Nanotechnology Infrastructure of UCSD, which is supported by NSF ECCS-1542148. N.E. and J.D.A. are grateful for support from the Air Force Office of Scientific Research (Grant FA9550-17-1-0261) and NSF OIA-1757220.

REFERENCES

(1) Rogalski, A. In *Next Decade in Infrared Detectors*, Proceedings Volume 10433, 2017; p 104330L.

(2) Pelayo García de Arquer, F.; Armin, A.; Meredith, P.; Sargent, E. H. Solution-Processed Semiconductors for next-Generation Photodetectors. *Nat. Rev. Mater.* **2017**, *2*, No. 16100.

(3) Carr, J. A.; Franke, D.; Caram, J. R.; Perkinson, C. F.; Saif, M.; Askoxylakis, V.; Datta, M.; Fukumura, D.; Jain, R. K.; Bawendi, M. G.; Bruns, O. T. Shortwave Infrared Fluorescence Imaging with the Clinically Approved Near-Infrared Dye Indocyanine Green. *Proc. Natl. Acad. Sci. U.S.A.* **2018**, *115*, 4465.

(4) Dou, L.; Liu, Y.; Hong, Z.; Li, G.; Yang, Y. Low-Bandgap Near-IR Conjugated Polymers/Molecules for Organic Electronics. *Chem. Rev.* **2015**, *115*, 12633−12665.

(5) Wu, Z.; Zhai, Y.; Kim, H.; Azoulay, J. D.; Ng, T. N. Emerging Design and Characterization Guidelines for Polymer-Based Infrared Photodetectors. *Acc. Chem. Res.* **2018**, *51*, 3144−3153.

(6) Benduhn, J.; Tvingstedt, K.; Piersimoni, F.; Ullbrich, S.; Fan, Y.; Tropiano, M.; McGarry, K. A.; Zeika, O.; Riede, M. K.; Douglas, C. J.;

DOI: 10.1021/acsami.9b08622
ACS Appl. Mater. Interfaces 2019, 11, 36880−36885

Barlow, S.; Marder, S. R.; Neher, D.; Spoltore, D.; Vandewal, K. Intrinsic Non-Radiative Voltage Losses in Fullerene-Based Organic Solar Cells. *Nat. Energy* **2017**, *2*, No. 17053.

(7) Wu, Z.; Yao, W.; London, A. E.; Azoulay, J. D.; Ng, T. N. Elucidating the Detectivity Limits in Shortwave Infrared Organic Photodiodes. *Adv. Funct. Mater.* **2018**, *28*, No. 1800391.

(8) Baeg, K. J.; Binda, M.; Natali, D.; Caironi, M.; Noh, Y. Y. Organic Light Detectors: Photodiodes and Phototransistors. *Adv. Mater.* **2013**, *25*, 4267−4295.

(9) Jansen-van Vuuren, R. D.; Armin, A.; Pandey, A. K.; Burn, P. L.; Meredith, P. Organic Photodiodes: The Future of Full Color Detection and Image Sensing. *Adv. Mater.* **2016**, *28*, 4766−4802.

(10) Xu, H.; Li, J.; Leung, B. H. K. K.; Poon, C. C. Y. Y.; Ong, B. S.; Zhang, Y.; Zhao, N. A High-Sensitivity near-Infrared Phototransistor Based on an Organic Bulk Heterojunction. *Nanoscale* **2013**, *5*, 11850−11855.

(11) Caranzi, L.; Pace, G.; Sassi, M.; Beverina, L.; Caironi, M. Transparent and Highly Responsive Phototransistors Based on a Solution-Processed, Nanometers-Thick Active Layer, Embedding a High-Mobility Electron-Transporting Polymer and a Hole-Trapping Molecule. *ACS Appl. Mater. Interfaces* **2017**, *9*, 28785−28794.

(12) Milvich, J.; Zaki, T.; Aghamohammadi, M.; Rödel, R.; Kraft, U.; Klauk, H.; Burghartz, J. N. Flexible Low-Voltage Organic Phototransistors Based on Air-Stable Dinaphtho[2,3-b:2′,3′-f]Thieno[3,2-b]Thiophene (DNTT). *Org. Electron.* **2015**, *20*, 63−68.

(13) Pierre, A.; Gaikwad, A.; Arias, A. C. Charge-Integrating Organic Heterojunction Phototransistors for Wide-Dynamic-Range Image Sensors. *Nat. Photonics* **2017**, *11*, 193−199.

(14) Rim, Y. S.; Yang, Y. M.; Bae, S.; Chen, H.; Li, C.; Goorsky, M. S.; Yang, Y. Ultrahigh and Broad Spectral Photodetectivity of an Organic − Inorganic Hybrid Phototransistor for Flexible Electronics. *Adv. Mater.* **2015**, *27*, 6885−6891.

(15) Tak, Y. J.; Kim, D. J.; Kim, W. G.; Lee, J. H.; Kim, S. J.; Kim, J. H.; Kim, H. J. Boosting Visible Light Absorption of Metal-Oxide-Based Phototransistors via Heterogeneous In-Ga-Zn-O and $CH_3NH_3PbI_3$ Films. *ACS Appl. Mater. Interfaces* **2018**, *10*, 12854−12861.

(16) Zhang, Y.; Yuan, Y.; Huang, J. Detecting 100 fW cm^{-2} Light with Trapped Electron Gated Organic Phototransistors. *Adv. Mater.* **2017**, *29*, No. 1603969.

(17) Xie, C.; You, P.; Liu, Z.; Li, L.; Yan, F. Ultrasensitive Broadband Phototransistors Based on Perovskite/Organic-Semiconductor Vertical Heterojunctions. *Light: Sci. Appl.* **2017**, *6*, No. e17023.

(18) Shen, L.; Lin, Y.; Bao, C.; Bai, Y.; Deng, Y.; Wang, M.; Li, T.; Lu, Y.; Gruverman, A.; Li, W.; HuaNg, J. Integration of Perovskite and Polymer Photoactive Layers to Produce Ultrafast Response, Ultraviolet-to-near-Infrared, Sensitive Photodetectors. *Mater. Horiz.* **2017**, *4*, 242−248.

(19) Rim, Y. S.; Ok, K. C.; Yang, Y. M.; Chen, H.; Bae, S. H.; Wang, C.; Huang, Y.; Park, J. S.; Yang, Y. Boosting Responsivity of Organic-Metal Oxynitride Hybrid Heterointerface Phototransistor. *ACS Appl. Mater. Interfaces* **2016**, *8*, 14665−14670.

(20) Jiang, J.; Ling, C.; Xu, T.; Wang, W.; Niu, X.; Zafar, A.; Yan, Z.; Wang, X.; You, Y.; Sun, L.; Lu, J.; Wang, J.; Ni, Z. Defect Engineering for Modulating the Trap States in 2D Photoconductors. *Adv. Mater.* **2018**, No. 1804332.

(21) Konstantatos, G.; Badioli, M.; Gaudreau, L.; Osmond, J.; Bernechea, M.; de Arquer, F. P. G.; Gatti, F.; Koppens, F. H. L. Hybrid Graphene−Quantum Dot Phototransistors with Ultrahigh Gain. *Nat. Nanotechnol.* **2012**, *7*, 363.

(22) Han, J.; Yang, D.; Ma, D.; Qiao, W.; Wang, Z. Y. Low - Bandgap Polymers for High - Performance Photodiodes with Maximal Low-Bandgap Polymers for High-Performance Photodiodes with Maximal EQE near 1200 nm and Broad Spectral Response from 300 to 1700 nm. *Adv. Opt. Mater.* **2018**, *6*, No. 1800038.

(23) Furchi, M. M.; Polyushkin, D. K.; Pospischil, A.; Mueller, T. Mechanisms of Photoconductivity in Atomically Thin MoS_2. *Nano Lett.* **2014**, *14*, 6165−6170.

(24) Torabi, S.; Jahani, F.; Van Severen, I.; Kanimozhi, C.; Patil, S.; Havenith, R. W. A.; Chiechi, R. C.; Lutsen, L.; Vanderzande, D. J.; Cleij, T. J.; Hummelen, J. C.; Koster, L. J. A. Strategy for Enhancing the Dielectric Constant of Organic Semiconductors without Sacrificing Charge Carrier Mobility and Solubility. *Adv. Funct. Mater.* **2015**, *25*, 150−157.

(25) Constantinou, I.; Yi, X.; Shewmon, N. T.; Klump, E. D.; Peng, C.; Garakyaraghi, S.; Lo, C. K.; Reynolds, J. R.; Castellano, F. N.; So, F. Effect of Polymer-Fullerene Interaction on the Dielectric Properties of the Blend. *Adv. Energy Mater.* **2017**, *7*, No. 1601947.

(26) Wu, Z.; Zhai, Y.; Yao, W.; Eedugurala, N.; Zhang, S.; Huang, L.; Gu, X.; Azoulay, J. D.; Ng, T. N. The Role of Dielectric Screening in Organic Shortwave Infrared Photodiodes for Spectroscopic Image Sensing. *Adv. Funct. Mater.* **2018**, *28*, No. 1805738.

(27) Leblebici, S.; Lee, J.; Weber-Bargioni, A.; Ma, B. Dielectric Screening to Reduce Charge Transfer State Binding Energy in Organic Bulk Heterojunction Photovoltaics. *J. Phys. Chem. C* **2017**, *121*, 3279−3285.

(28) Kim, H.; Ng, T. N. Reducing Trap States in Printed Indium Zinc Oxide Transistors by Doping with Benzyl Viologen. *Adv. Electron. Mater.* **2018**, *4*, No. 1700631.

(29) Street, R. A.; Ng, T. N.; Lujan, R. A.; Son, I.; Smith, M.; Kim, S.; Lee, T.; Moon, Y.; Cho, S. Sol-Gel Solution-Deposited InGaZnO Thin Film Transistors. *ACS Appl. Mater. Interfaces* **2014**, *6*, 4428−4437.

(30) Jeon, S.; Ahn, S. E.; Song, I.; Kim, C. J.; Chung, U. I.; Lee, E.; Yoo, I.; Nathan, A.; Lee, S.; Robertson, J.; et al. Gated Three-Terminal Device Architecture to Eliminate Persistent Photoconductivity in Oxide Semiconductor Photosensor Arrays. *Nat. Mater.* **2012**, *11*, 301−305.

(31) Leblebici, S. Y.; Chen, T. L.; Olalde-Velasco, P.; Yang, W.; Ma, B. Reducing Exciton Binding Energy by Increasing Thin Film Permittivity: An Effective Approach to Enhance Exciton Separation Efficiency in Organic Solar Cells. *ACS Appl. Mater. Interfaces* **2013**, *5*, 10105−10110.

(32) Ng, T. N.; Chabinyc, M. L.; Street, R. A.; Salleo, A. In *Bias Stress Effects in Organic Thin Film Transistors*, IEEE International Reliability Physics Symposium, Phoenix, 2007; pp 243−247.

(33) Bisquert, J.; Bertoluzzi, L.; Mora-Sero, I.; Garcia-Belmonte, G. Theory of Impedance and Capacitance Spectroscopy of Solar Cells with Dielectric Relaxation, Drift-Diffusion Transport, and Recombination. *J. Phys. Chem. C* **2014**, *118*, 18983−18991.

(34) Macdonald, D.; Cuevas, A. Trapping of Minority Carriers in Multicrystalline Silicon. *Appl. Phys. Lett.* **1999**, *74*, 1710−1712.

(35) Rogalski, A.; Bielecki, Z. Detection of Optical Radiation. *Bull. Pol. Acad. Sci.: Tech. Sci.* **2004**, *52*, 43−66.

(36) Ng, T. N.; Schwartz, D. E.; Mei, P.; Kor, S.; Veres, J.; Bröms, P.; Karlsson, C. Pulsed Voltage Multiplier Based on Printed Organic Devices. *Flexible Printed Electron.* **2016**, *1*, No. 015002.

(37) London, A.; Huang, L.; Zhang, B.; Oviedo, B.; Tropp, J.; Yao, W.; Wu, Z.; Wong, B.; Ng, T. N.; Azoulay, J. D. Donor−Acceptor Polymers with Tunable Infrared Photoresponse. *Polym. Chem.* **2017**, *8*, 2922−2930.

(38) Wu, Z.; Yao, W.; London, A. E.; Azoulay, J. D.; Ng, T. N. Temperature-Dependent Detectivity of Near-Infrared Organic Bulk Heterojunction Photodiodes. *ACS Appl. Mater. Interfaces* **2017**, *9*, 1654−1660.

(39) Yao, W.; Wu, Z.; Huang, E.; Huang, L.; London, A. E.; Liu, Z.; Azoulay, J. D.; Ng, T. N. Organic Bulk Heterojunction Infrared Photodiodes for Imaging Out to 1300 nm. *ACS Appl. Electron. Mater.* **2019**, *1*, 660−666.

DOI: 10.1021/acsami.9b08622
ACS Appl. Mater. Interfaces 2019, 11, 36880−36885